Applied Catalysis B: Environmental 160–161 (2014) 566–573

Contents lists available at ScienceDirect

Applied Catalysis B: Environmental

journal homepage: www.elsevier.com/locate/apcatb

Mesoporous Ce—Pr—O solid solution with efficient photocatalytic activity under weak daylight irradiation

Shiyou Hao[a,*], Jie Hou[b], Paolo Aprea[c], Francesco Pepe[d]

[a] Xingzhi College, Zhejiang Normal University, 321004 Jinhua, PR China
[b] College of Chemistry and Life Sciences, Zhejiang Normal University, 321004 Jinhua, PR China
[c] Department of Chemical, Materials and Production Engineering, University Federico II, P.le V. Tecchio 80, 80125 Naples, Italy
[d] Department of Engineering, University of Sannio, Piazza Roma 21, 82100 Benevento, Italy

ARTICLE INFO

Article history:
Received 13 April 2014
Received in revised form 2 June 2014
Accepted 8 June 2014
Available online 13 June 2014

Keywords:
Mesoporous Ce—Pr—O
Rhodamine B
Degradation
Weak daylight photocatalysis
Photodegradation mechanism

ABSTRACT

In this study, the application of mesoporous CeO_2 and Pr doped CeO_2 (Ce—Pr—O) as photocatalysts for the degradation of Rhodamine B (RhB) from aqueous solution was investigated. Mesoporous CeO_2 and Ce—Pr—O were prepared using SBA-15 as template. The resultant samples were characterized by XRD, N_2 adsorption–desorption, Raman, UV–vis, TEM, FT-IR, and XPS techniques. The characterization results show that the synthesized Ce—Pr—O has a 2D hexagonal structure, similar to that of the template, and possesses numerous oxygen vacancies. It is worth mentioning that the visible light adsorption intensity of Ce—Pr—O is much higher than that of mesoporous ceria and bulk ceria, due to simultaneous formation of doping level and mesopores. The photodegradation of RhB illustrates that the synthesized mesoporous Ce—Pr—O, especially 45% Ce—Pr—O, performs excellent decolorization under weak daylight irradiation. Furthermore, a novel photodegradation mechanism was proposed based on the adsorption of H_2O_2 over the oxygen vacancy.

1. Introduction

Fluorite-structured ceria (CeO_2) and ceria-based compounds are attractive materials due to their extensive applications as catalysts [1], oxygen sensors [2], UV blockers [3], polishing powders [4], etc. As shown by Fallah et al., CeO_2 can be photoactivated by near UV–vis irradiation [5], implying that it is likely to be a promising photocatalyst. Recently, many researches have focused on the photocatalytic properties of ceria and ceria-based compounds [6–8]. It is well known that ceria, with a 3.2 eV bandgap, has a strong absorption in the region of UV light. However, the absorption intensity in the region of visible light is relatively lower. In order to improve the photocatalytic activity of CeO_2 under visible light or solar irradiation, two methods, i.e., enhancing surface area and doping with other metallic oxides, are generally applied [9,10].

As reported by Ji et al., compared with bulk CeO_2, mesoporous CeO_2 with a larger surface area showed a much higher photodegradation activity under otherwise identical conditions [11]. Ji and coworkers successfully loaded CeO_2 onto reduced graphene oxide, greatly enhancing the surface area and thus efficiently improving the photocatalytic activity of the CeO_2 nanoparticles [12]. On the other hand, better photocatalytic activities are often obtained with ceria-based compounds, generally produced by doping ceria with other metallic oxides. A p–n junction photocatalyst obtained by doping CeO_2 (a n-type semiconductor) with a p-type semiconductor such as Cu_2O has a much higher photocatalytic activity because it can separate the photogenerated electrons and holes efficiently and improve the visible light absorption [13]. Recently, Cai et al. proposed a hydrothermal method for the synthesis of Fe^{3+} doped ceria and investigated its photodegradation properties [14]. They found that the adsorption capacity as well as the catalytic degradation of acid orange 7 under visible light irradiation was greatly enhanced because the doping increased the concentration of Ce^{3+}. Similar results were also found by Channei et al., who prepared Fe-doped CeO_2 nanoparticles by flame spray pyrolysis [15].

Although the photocatalytic activity of ceria can be enhanced by improving surface area and/or doping with other oxides, the absorption in the range of visible light is still scarce, reducing the yield of photogenerated electrons and holes. Moreover, ceria and ceria-based photocatalysts have to be irradiated under sunlight or artificial visible light to excite electrons during the photocatalysis [16,17], which greatly limits their practical applications. It is well known that photocatalysts with mesopore channels not only facilitate fast intraparticle molecular transfer but also enhance the

* Corresponding author. Tel.:+86 579 82287468; fax: +86 579 82287468.
E-mail address: sky54@zjnu.cn (S. Hao).

http://dx.doi.org/10.1016/j.apcatb.2014.06.013
0926-3373/

light harvesting and improve the adsorption of reactant molecules [18]. On the other hand, doping with other metallic oxides can effectively extend the photo-response of CeO_2 in the visible light region and enhance the photocatalytic efficiency under visible light irradiation. Based on the above considerations, we can infer that the photocatalytic activity of ceria can be enhanced greatly via doping with other metallic oxides and using a mesoporous structure, simultaneously.

Compared with other metal ions such as Fe^{3+} and Cu^{+}, lower valence Pr-ions are considered to be among the most promising candidates to either substitute Ce-ions or enter the interstices of the crystal lattice of CeO_2 due to their ionic radii, similar to those of Ce-ions, and the particular f and d electron orbital structure, which greatly reduces the bandgap of ceria and thus improves its photocatalytic properties. To the best of our knowledge, there are only few reports about the synthesis of mesoporous Ce—M—O (M = other metallic element) composites, especially for Ce—Pr—O system with different compositions and their activity toward photocatalytic degradation of organic pollutants.

In this work, mesoporous Ce—Pr—O solid solutions with remarkable absorption of visible light were synthesized using a large pore size SBA-15 (6.5 nm) as hard template, because the precursor can easily go into the template matrix and the copy of the hard template at mesoscale is convenient to achieve [11]. The catalytic degradation of Rhodamine B (RhB), a fluorescent dye, was employed as a model reaction to evaluate the catalytic activity of the mesoporous Ce—Pr—O under weak natural light irradiation at lab scale. The results showed that the prepared mesoporous Ce—Pr—O was effective for the degradation of RhB under natural light irradiation, indicating a good photocatalytic activity in view of its practical applications. Furthermore, a novel photocatalytic mechanism was proposed.

2. Experimental

2.1. Chemicals

Tetraethylorthosilicate (TEOS, 98%, Acros Organics) and Pluronics P123 ($EO_{20}PO_{70}EO_{20}$, average molecular weight: 5800, Sigma-Aldrich) were used as silica source and surfactant, respectively. $Ce(NO_3)_3{\cdot}6H_2O$, $Pr(NO_3)_3{\cdot}6H_2O$, NaOH, $KMnO_4$, 98% concentrated sulfuric acid, 37% fuming hydrochloric acid, absolute ethanol, and Rhodamine B were purchased from Sinopharm Chemical Reagent Co. All the chemical reagents were used without further purification. 2.0 (0.1) M of HCl solution was prepared from the 37% fuming hydrochloric acid. 1 M of H_2SO_4 solution was synthesized from the 98% concentrated sulfuric acid. Deionized water with a resistivity larger than 18.2 MΩ was obtained from Millipore Milli-Q® ultrapure water purification systems.

2.2. Synthesis

The ordered mesoporous SBA-15 template was prepared by a method reported in our previous study [19]. Typically, 2.4 g of P123 was dissolved in 72 g of 2.0 M HCl solution at room temperature, followed by adding 18 g of deionized water. Then a calculated amount of TEOS was added into the above-prepared solution. Afterwards the resulting mixture was stirred at 40 °C for 24 h, then transferred into a Teflon autoclave, and the synthesis was carried out without agitation in an oven at 90 °C for 24 h. The product was filtered and the solid was washed with deionized water. The washed solid was then dried at 60 °C overnight prior to a further analysis or use. The template was removed from the as-synthesized material by an extraction with ethanol.

A typical synthesis of mesoporous Ce—Pr—O is presented as follows: 2.5 g of $Ce(NO_3)_3{\cdot}6H_2O$ and a certain amount of $Pr(NO_3)_3{\cdot}6H_2O$ were dissolved in sequence into 15 ml of absolute ethanol at room temperature (different samples were prepared having the following $Pr(NO_3)_3{\cdot}6H_2O/Ce(NO_3)_3{\cdot}6H_2O$ mass ratios: 0, 5, 25, 45, 55%). After the solution became clear, 1.0 g of SBA-15 was added and the suspension was vigorously stirred at 70 °C to evaporate ethanol. Afterwards, the Ce—Pr precursor/silica composite was calcined in air at 500 °C for 3 h with a heating ramp of 1 °C min^{-1} to produce a Ce—Pr—Si—O compound oxide. In order to achieve higher loadings, the above impregnation step was repeated with half the amount of precursors. The resulting samples were calcined again using the same way as before to completely decompose the inorganic precursors. Finally, the SBA-15 template was removed etching the sample with 3 M NaOH solution at 60 °C for 15 min. The etching process was repeated four times. Based on the initial $Pr(NO_3)_3{\cdot}6H_2O/Ce(NO_3)_3{\cdot}6H_2O$ mass ratios, the obtained Ce—Pr—O composites are hereafter denoted as CeO_2, 5%Ce—Pr—O, 25%Ce—Pr—O, 45%Ce—Pr—O and 55%Ce—Pr—O, respectively.

2.3. Characterization

The X-ray diffraction (XRD) patterns were collected on a Philips PW3040/60 powder diffractometer using Cu $K\alpha$ radiation (λ = 0.154 nm). The adsorption isotherms of N_2 were measured with a Micromeritics ASAP 2020 apparatus at −196 °C and the specific surface areas of the investigated samples were calculated using the multiple-point Brunauer–Emmett–Teller (BET) method in the relative pressure range p/p_0 = 0.05–0.3. Transmission electron microscopy (TEM) images were acquired using a 2100 JEOL electron microscope with an acceleration voltage of 200 kV. The diffuse reflectance spectra of the samples over a range of 200–800 nm were recorded by a Nicolet Evolution 500 Scan UV–vis system. Raman scattering analysis was performed on a Renishaw RM1000 Raman spectrometer with a 514 nm excitation laser light. The FT-IR spectra were recorded by a Nicole Nexus 670 spectrometer with a resolution of 4 cm^{-1} using the KBr pellet method. X-ray photoelectron spectroscopy (XPS) measurement was carried out on a RBO upgraded PHI-5000 C ESCA system (Perkin Elmer) using monochromated Al $K\alpha$ X-rays (E = 1486.6 eV) as a radiation at 250 W. All binding energies were calibrated using carbon (C_{1S} = 284.6 eV) as a reference. The concentration of Ce or Pr in the solid solution was measured by a PerkinElmer optima 2100 DV atomic emission spectrometer.

2.4. Photocatalytic tests

The photocatalytic activities of CeO_2 and Ce—Pr—O mesoporous samples were evaluated by the photodegradation of RhB. Typically, 25 ml of RhB solution at different concentrations (ranging from 25 to 110 mg/l) and 25 mg of CeO_2 or Ce—Pr—O powder were placed in a beaker under vigorous agitation. The pH value of all the solutions containing RhB used for the photocatalytic experiments was adjusted to the desired one using 0.1 M HCl. Afterwards, the suspensions were stirred in the dark for 1 h to reach the adsorption–desorption equilibrium. Then 1 mmol of 37% H_2O_2 solution was added to the mixture under the laboratory natural light as light source. At given time intervals a small amount of suspension was withdrawn and centrifuged to remove the photocatalyst. The residual RhB levels in the filtrates were then analyzed by recording the variations of the absorbance at 552 nm with a UV–vis spectrophotometer (Evolution 500LC). The degradation efficiency of RhB was evaluated as C/C_0, where C_0 is the initial concentration of RhB (mg/l) and C is the concentration of RhB (mg/l) in the filtrates.

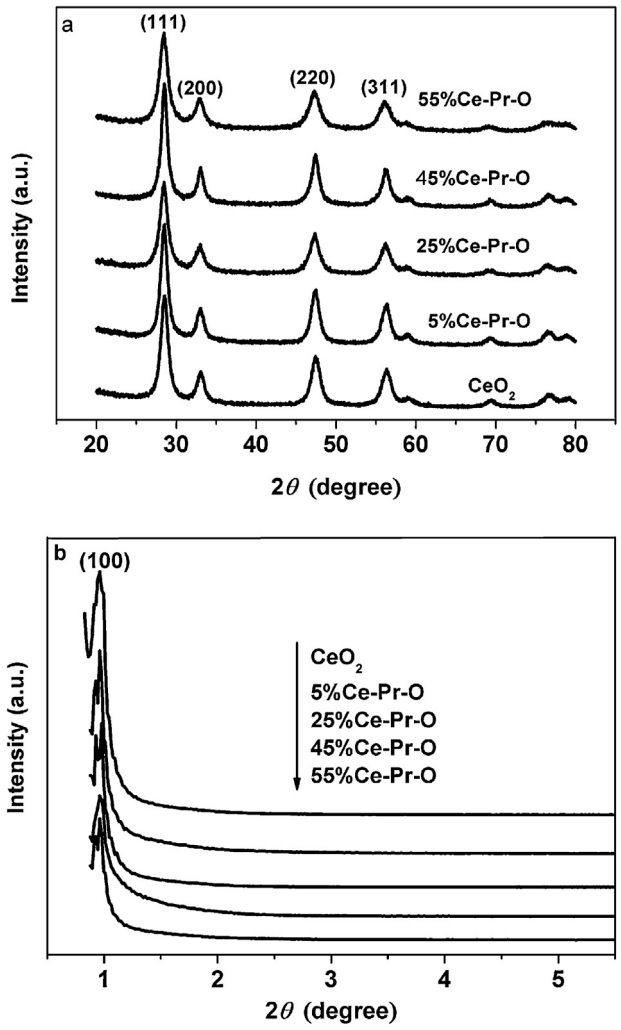

Fig. 1. Wide-angle (a) and low-angle (b) XRD patterns of mesoporous CeO_2, 5%Ce—Pr—O, 25%Ce—Pr—O, 45%Ce—Pr—O and 55%Ce—Pr—O.

2.5. Evaluation of H_2O_2 adsorption

The adsorption of H_2O_2 on the mesoporous CeO_2 and Ce—Pr—O was carried out *via* the following procedure. First, 25 ml of aqueous solution containing 0.05 g of mesoporous CeO_2 or Ce—Pr—O was placed in a beaker under vigorous agitation. The pH of the solution was kept at a value of about 7 using 0.1 M NaOH or HCl to avoid the reaction between H_2O_2 and CeO_2 or Ce—Pr—O. Afterwards, 1 ml of 30% H_2O_2 was added and the mixture was stirred vigorously for 1 h to reach the adsorption–desorption equilibrium. Finally, the mesoporous CeO_2 or Ce—Pr—O was filtered and then washed with deionized water for three times. The residual H_2O_2 levels in the filtrate were titrated by a 0.1 M of $KMnO_4$ in 1 M sulfuric acid solution.

3. Results and discussion

3.1. Textural and physicochemical properties

Fig. 1 shows the powder X-ray diffraction (XRD) patterns of mesoporous CeO_2 and Ce—Pr—O compounds. Crystalline phases were identified in comparison with the cubic CeO_2 ICDD file (PDF no. 81-0792). From Fig. 1a, it can be seen that the structure of all samples is fluorite-like, and the diffraction peaks are very close to each other, implying the formation of a Ce—Pr—O solid solution. The low-angle XRD patterns in Fig. 1b show that a high diffraction peak at around 0.96 degree (the characteristic diffraction peak indexed to (1 0 0) reflection of the SBA-15 template) for all samples, indicating the synthesized CeO_2 and Ce—Pr—O composites have retained a relatively regular mesostructure.

To further identify the mesostructure, especially the mesopore arrangement of all the samples, TEM observations were performed and the images of SBA-15 and 45%Ce—Pr—O are presented in Fig. 2. In Fig. 2a, a parallel orientation of channels along the long axis of the template (SBA-15) can be clearly observed, suggesting that SBA-15 template has a finely ordered 2D-channel mesostructure. From the low magnification TEM image of 45%Ce—Pr—O (Fig. 2b), a ordered 2D hexagonal mesostructure can be easily found, indicating that the prepared Ce—Pr—O solid solution is a good reverse-replica of the template, in good agreement with the low-angle XRD result. A similar structure to that of 45%Ce—Pr—O is also observed for CeO_2, 25%Ce—Pr—O, and 55%Ce—Pr—O (not shown).

Fig. 3 depicts the adsorption–desorption isotherms of N_2 on CeO_2 and Ce—Pr—O compounds at −196 °C. From Fig. 3, it can be seen that all isotherms display a type IV isotherm with a hysteresis loop between type H3 and H4 [11]. It should be noted that all isotherms exhibit the N_2 capillary condensation in a wide range of relative pressure (P/P_0 = 0.5–0.95), characteristic of the mesoporous structure. The corresponding textural properties are summarized in Table 1. It can be seen from Table 1 that the BET surface area of mesoporous CeO_2 and Ce—Pr—O materials ranges from 109 to 135 m^2/g and the corresponding pore volume varies between 0.21 and 0.34 cm^3/g. From Table 1, it can be also found that the atomic ratio of Pr to Ce in the final sample is similar to that of the initial compound.

The Raman spectra for mesoporous CeO_2, 5%Ce—Pr—O, 25%Ce—Pr—O, 45%Ce—Pr—O and 55%Ce—Pr—O are shown in Fig. 4. For the pure mesoporous CeO_2, a strong band at 463 cm^{-1} can be clearly detected, which has been ascribed to the Raman active F_{2g} mode of CeO_2, the band of a fluorite isostructural material [20,21].

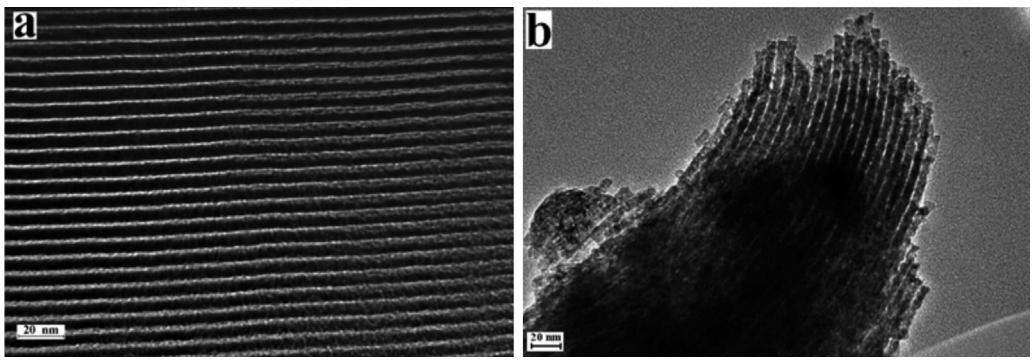

Fig. 2. TEM images of template (a) and 45%Ce—Pr—O (b).

Table 1
Textural and physicochemical properties of *m*-CeO_2, 5%Ce—Pr—O, 25%Ce—Pr—O, 45%Ce—Pr—O and 55%Ce—Pr—O.

Sample code	Initial Pr/Ce atomic (%)	Final Pr/Ce atomic (%)	S_{BET} (m^2/g)	D_A (nm)	V_{total} (cm^3/g)
m-CeO_2	0	0	121	7.66	0.28
5%Ce—Pr—O	5	4.96	118	10.25	0.34
25%Ce—Pr—O	25	24.86	135	7.61	0.27
45%Ce—Pr—O	45	44.85	128	7.50	0.28
55%Ce—Pr—O	55	54.94	109	7.01	0.21

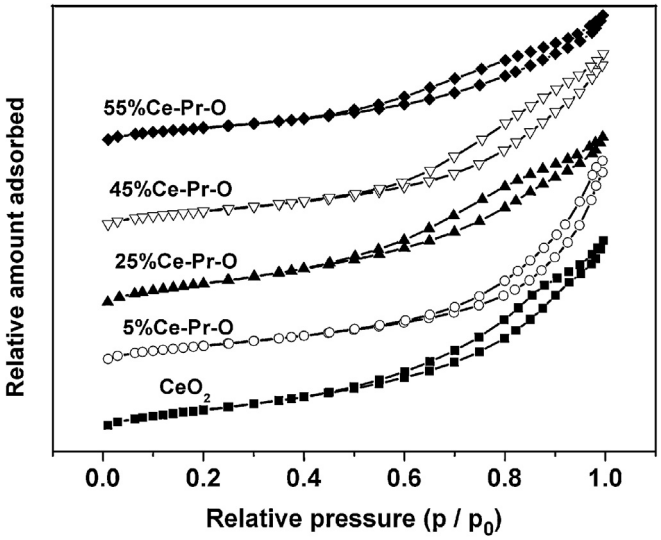

Fig. 3. N_2 adsorption–desorption isotherms of mesoporous CeO_2, 5%Ce—Pr—O, 25%Ce—Pr—O, 45%Ce—Pr—O and 55%Ce—Pr—O at −196 °C.

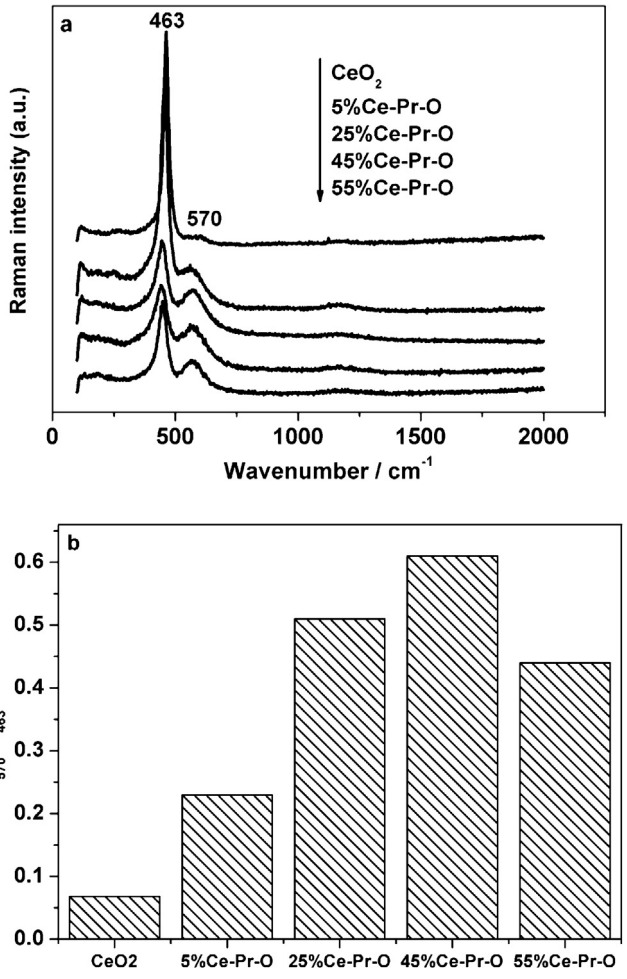

Fig. 4. (a) Raman spectra of CeO_2 and Ce—Pr—O (all the curves are setoff along the *y* axis for clarity), and (b) the corresponding I_{570}/I_{463} ratios.

However, this band broadens and its intensity gradually decreases with increasing the Pr doping. A similar result was reported by Cai et al. when they doped ceria with Fe^{3+} [14]. The reason may be that the presence of Pr produces a distortion in the lattice of the CeO_2 crystals, perturbing the vibrations of the lattice. The weak peak at around 570 cm^{-1} can be associated to oxygen vacancies [20] and its intensity increases with the Pr doping, implying that the concentration of oxygen vacancies in the Ce—Pr—O is higher. In order to determine the relationship between the oxygen vacancy concentration and the Pr doping amount, the ratio I_{570}/I_{463} of the Raman band intensity at 570 cm^{-1} (I_{570}) to that at 463 cm^{-1} (I_{463}) is taken representative of the oxygen vacancy concentration. [22] The evolution of I_{570}/I_{463} as a function of the different Pr doping amounts in the Ce—Pr—O is presented in Fig. 4b, which suggests a Pr doping value of 45% as the optimum in order to maximize the oxygen vacancy concentration. In particular, I_{570}/I_{463} varies from 0.23 to 0.61, much higher than 0.07 of FC10 reported by Cai et al. [14], implying that plentiful oxygen vacancies were formed in the Ce—Pr—O. Furthermore, the I_{570}/I_{463} value of mesoporous CeO_2 (0.068) is much higher than that of bulk CeO_2 (0.005), indicating that the formation of mesopores is beneficial to increase the concentration of oxygen vacancy.

The formation of oxygen vacancies in the mesoporous Ce—Pr—O can be further deduced from the XPS results. Fig. 5 shows the XPS spectra of Ce 3d (a) and Pr 3d (b) orbitals of the 45%Ce—Pr—O. From Fig. 5a, the presence of Ce^{4+} in the solid solution is confirmed by the peaks at 916.5, 900.6, 898.2, 888.7, and 882.4 eV. It can also be found from Fig. 5a that there is a small amount of Ce^{3+} at the surface of Ce—Pr—O. The valence state of Pr is mainly +3 and between +3 and +4, which can be proved by Fig. 5b. The peak around 933.2 eV can be ascribed to the Pr^{3+} $3d_{5/2}$, while those located around 953.7 and 973.2 eV are likely to be Pr_2O_3 and/or Pr_6O_{11} [23]. Therefore, we can conclude that the formation of oxygen vacancies is due to the fact that Ce^{4+} is replaced by lower valence state ions such as Ce^{3+}, Pr^{3+}, which can be expressed by the following equations:

$$CeO_2 \rightarrow Ce_{1-x}(IV) \cdot Ce_x(III) \cdot O_{2-x/2} \cdot \left(\frac{x}{2}\right) V_O^{\bullet\bullet} + \left(\frac{x}{4}\right) O_2 \quad (1)$$

$$CeO_2 \rightarrow Ce_{1-y}(IV) \cdot Pr_y(III) \cdot O_{2-y/2} \cdot \left(\frac{y}{2}\right) V_O^{\bullet\bullet} + \left(\frac{y}{4}\right) O_2 \quad (2)$$

where $V_O^{\bullet\bullet}$ represents oxygen vacancy.

In order to investigate the electronic states of the catalysts, UV–vis diffuse reflectance spectroscopy (DRS) studies were performed (shown in Fig. 6). For comparison purposes, a commercial bulk ceria (b-CeO_2) was also analyzed and plotted in Fig. 6. It can be seen that b-CeO_2 has a strong absorption peak in the ultraviolet region and a relatively weak one in the visible light field. Interestingly, the UV absorption intensity of the mesoporous CeO_2 is enhanced, and the absorption displays a red shift of light compared to that of b-CeO_2. When the mesoporous CeO_2 is doped

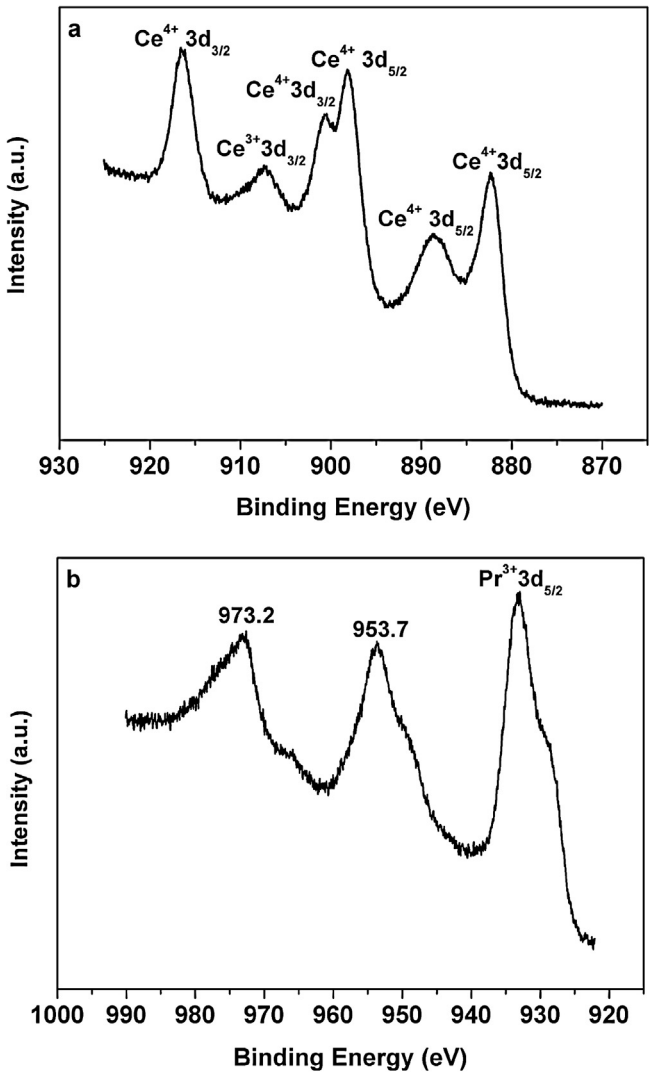

Fig. 5. XPS spectra of Ce 3d (a) and Pr 3d (b) in the mesoporous 45%Ce—Pr—O.

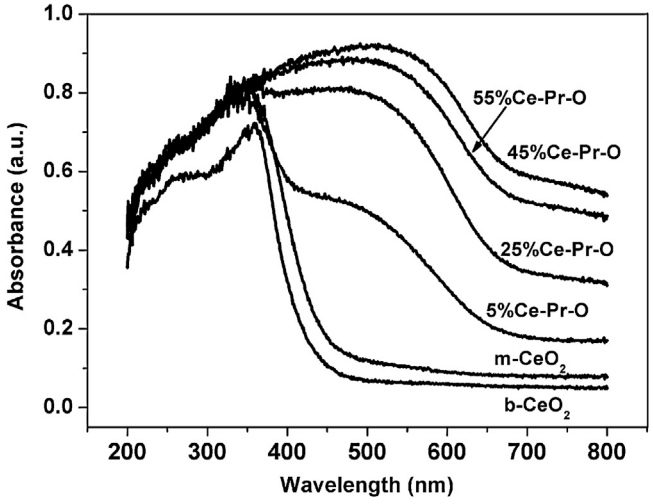

Fig. 6. Diffuse reflectance UV–vis spectra of pure CeO_2 and Ce—Pr—O (b-CeO_2: bulk CeO_2, *m*-CeO_2: mesoporous CeO_2).

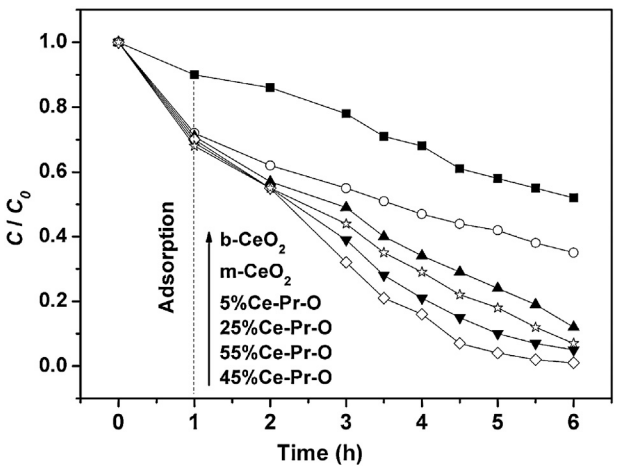

Fig. 7. The photodegradation of 25 mg/l RhB in the presence of different photocatalysts under weak daylight irradiation (pH = 4.5, $m_{photocatalyst}$ = 25 mg, V_{RhB} = 25 ml, $V_{H_2O_2}$ = 1 ml).

with Pr, the visible light absorption becomes much stronger, and the absorption intensity increases gradually with the Pr doping amount, then decreases after 45% of doping amount. This trend change is consistent with that of the oxygen vacancy concentration (OVC), implying that improving OVC is beneficial to the visible light absorption. Moreover, the stronger visible light absorption of mesoporous Ce—Pr—O may be ascribed to its texture, enlarged surface area and multiple scattering, which enable it to harvest light much more efficiently [24].

3.2. Photocatalytic activity

The photocatalytic activities of bulk CeO_2, mesoporous CeO_2 and Ce—Pr—O were evaluated for the degradation of RhB under weak daylight irradiation. Fig. 7 presents the photocatalytic degradation of RhB in the presence of the different samples. Compared with the bulk ceria, the mesoporous CeO_2 exhibit enhanced photocatalytic efficiency. It can be seen from Fig. 7 that the degradation fraction for the mesoporous CeO_2 is 65%, higher than that of 48% for the bulk CeO_2. According to Li et al., the enhanced photocatalytic activity of mesoporous materials is due to its physicochemical properties, such as crystal size, BET surface area, and pore structure [25]. From the TEM images, it is clear that the synthesized samples are nanometer sized, which allows for more efficient transfer of electron–holes generated inside the crystal to the surface. On the other hand, a large surface area not only supplies more active sites for the degradation of organic compounds, but also effectively promotes the separation efficiency of the electron–hole pairs, resulting in a higher quantum efficiency of the photocatalytic reaction [26]. Furthermore, such large pores in the mesoporous CeO_2 provide efficient transport paths for reactants and products in the photocatalytic reaction [27]. Compared with the mesoporous CeO_2, the mesoporous Ce—Pr—O solid solutions exhibit better performance on the degradation of RhB: it can be ascribed to the oxygen vacancies formed after Pr doping, as discussed from the results of the Raman analysis. Indeed, it is well known that oxygen vacancies, positively charged, can capture the photogenerated electrons, efficiently separating them from the holes. On the other hand, oxygen vacancies maybe improve the adsorption capacity of H_2O_2 on the surface of Ce—Pr—O due to the coordination interactions between oxygen vacancies and H_2O_2 (due to the electronegativity of the oxygen lone pair) and thus produce some intermediate products such as O_2^{2-} and/or $\{Ce(O_2)^+\}$ [28,29], which are then changed into active species to oxidize RhB. In order to estimate

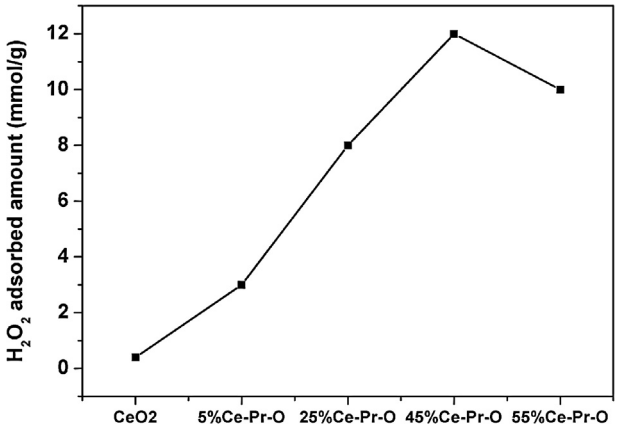

Fig. 8. H_2O_2 adsorbed amount on the mesoporous CeO_2 and Ce—Pr—O at the pH of 7.

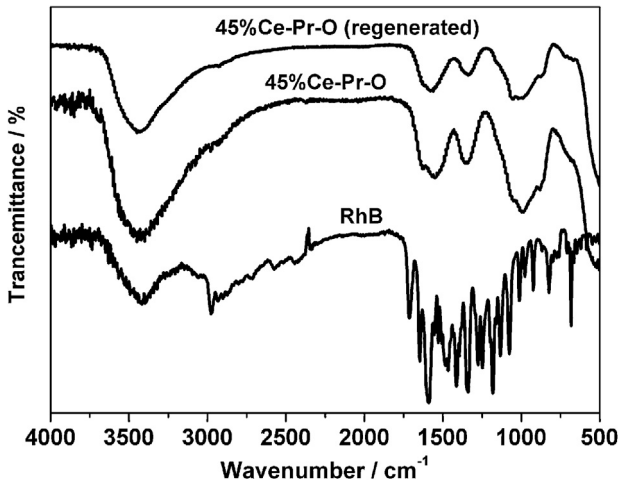

Fig. 10. FT-IR spectra of RhB, 45%Ce—Pr—O and the regenerated 45%Ce—Pr—O.

the effect of the oxygen vacancies on the adsorption of H_2O_2 on the Ce—Pr—O surface, we further performed a group of experiments and the results are presented in Fig. 8. It is easy to find from Fig. 8 that the adsorption amount increases with the oxygen vacancy concentration.

It is well known that, being the photocatalytic reaction carried out on the surface of the catalyst, the properties of its surface play an important role. It was reported that the pH of solution has great influence on the surface charge of the photocatalyst through the protonation of the free surface hydroxyl groups [30], as well as the degree of ionization and hydrolysis of the species presented in the solution [31]. The effect of pH on the degradation of 25 mg/l RhB over 45%Ce—Pr—O is shown in Fig. 9, from which it is obvious that the photocatalytic efficiency in acidic medium is higher than that in basic medium and that the degradation efficiency increases with decreasing pH. This is probably due to the fact that the hydroxyl groups on the surface of the catalyst are protonated under a pH value of 6.8 (the zero point of charge pH_{zpc} of CeO_2 is 6.8 [17]), which is helpful for improving the adsorption of organic species due to formation of hydrogen bonds and/or electrostatic interactions between the organic structure and protonated hydroxyl groups. On the other hand, H_2O_2 adsorbed on the catalyst surface can facilitate the recycle of Ce^{3+} and Ce^{4+} in the acidic medium, accompanying by the generation of O_2, which then capture photogenerated electrons to produce more active species such as hydroxyl radical and/or superoxide, according to the following equations:

$$H_2O_2 \rightarrow 2[OH^{\bullet}] \quad (3)$$

$$Ce_2O_3 + 2[OH^{\bullet}] \rightarrow 2CeO_2 + H_2O \quad (4)$$

$$2CeO_2 + 2H^+(aq) + H_2O_2 \rightarrow Ce_2O_3 + 1/2O_2 + 2H_2O \quad (5)$$

To further verify that RhB was actually degraded over the mesoporous photocatalysts, the FT-IR technique was employed. Fig. 10 shows the FT-IR spectra of RhB, 45%Ce—Pr—O and the regenerated 45%Ce—Pr—O recovered from the reaction solution by filtration. According to the literature [32], the vibrational modes of pure RhB are assigned as follows: the peak around 1697 cm^{-1} is ascribed to the stretching vibration band of the carboxylic group, the aromatic ring and heterocycle vibrations are in the region of 1450–1600 cm^{-1}, the 1334 cm^{-1} band is due to C-aryl bond vibrations, and the vibration of the carbon–nitrogen bond is present at about 1649 cm^{-1}. It is clearly seen from Fig. 10 that the FT-IR spectra of the regenerated 45%Ce—Pr—O is almost the same as that of the fresh one (in particular, no RhB peaks are detected), indicating that RhB was nearly photo degraded.

From Figs. 7 and 9, it is evident that 25 ml of 25 mg/l RhB can be almost degraded by 25 mg of 45%Ce—Pr—O under a pH of 4.5. Then, the same mass of Ce—Pr—O was tested under different experimental conditions. As an example, Fig. 11 presents the comparison

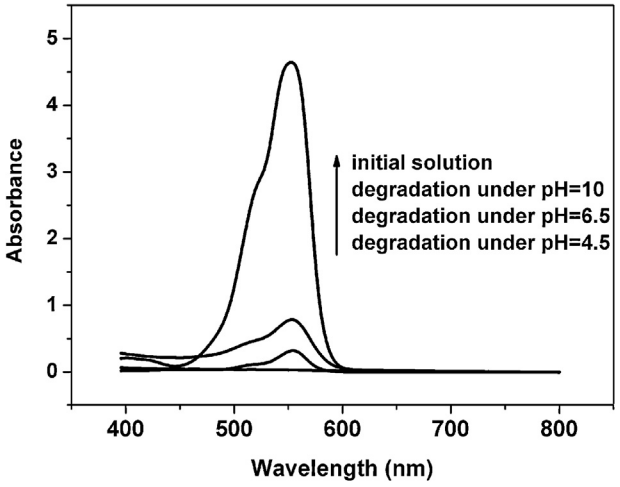

Fig. 9. Effect of pH on the degradation of 25 mg/l RhB over 45%Ce—Pr—O under weak daylight irradiation ($m_{45\%Ce-Pr-O}$ = 25 mg, V_{RhB} = 25 ml, $V_{H_2O_2}$ = 1 ml).

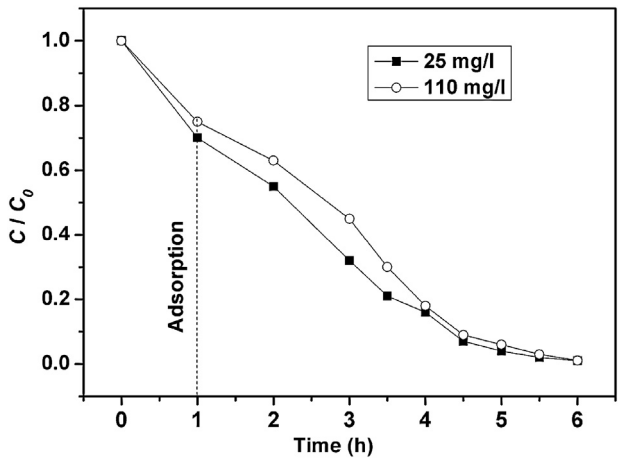

Fig. 11. The photodegradation of RhB with different concentration in the presence of 45%Ce—Pr—O under daylight irradiation (pH = 4.5, $m_{45\%Ce-Pr-O}$ = 25 mg, V_{RhB} = 25 ml, $V_{H_2O_2}$ = 1 ml).

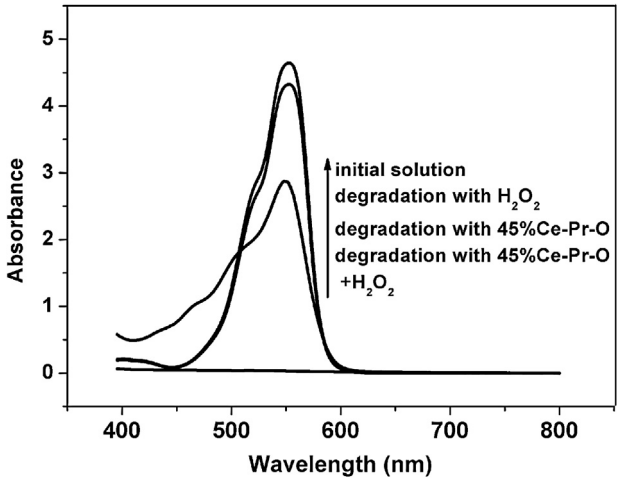

Fig. 12. Effect of H_2O_2 and Ce—Pr—O on the degradation of 25 mg/l RhB under daylight irradiation at pH of 4.5 ($m_{45\%Ce-Pr-O}$ = 25 mg, V_{RhB} = 25 ml, $V_{H_2O_2}$ = 1 ml).

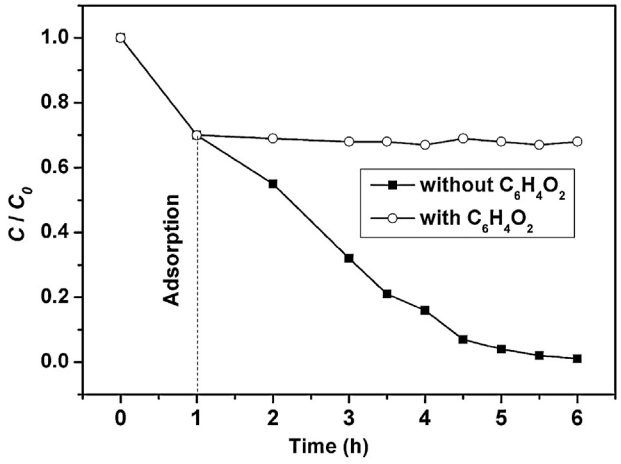

Fig. 13. Effect of $C_6H_4O_2$ on the degradation of 25 mg/l RhB (pH = 4.5, $m_{45\%Ce-Pr-O}$ = 25 mg, V_{RhB} = 25 ml, $V_{H_2O_2}$ = 1 ml, $C_{C_6H_4O_2}$ = 1 mM, $V_{C_6H_4O_2}$ = 0.5 ml).

between the photodegradation of RhB at 25 mg/l and 110 mg/l in presence of 45%Ce—Pr—O under weak daylight irradiation. It can be found from Fig. 11 that RhB is almost degraded when the concentration of RhB is up to 110 mg/l, suggesting that the mesoporous 45%Ce—Pr—O is highly efficient for the degradation of high concentrations of pollutants. Also, the catalytic degradation capacity of the mesoporous 45%Ce—Pr—O (expressed as the amount of pollutant degraded by 1 g of catalyst) turns out to be 110 mg/g, a much higher value than that of ordered mesoporous CeO_2 and Fe^{3+} doping CeO_2 (70 mg/g) [11,14], MO (=CuO, Co_3O_4, NiO)/$BiVO_4$ *p–n* junction composites (35 mg/g) [33], and carbon-coated CdS Petalous Nanostructures (20 mg/g) [34].

3.3. Photodegradation mechanism

Fig. 12 shows the effect of H_2O_2 and 45%Ce—Pr—O on the degradation of 25 mg/l RhB under weak daylight irradiation at pH of 4.5. It can be seen that only a small fraction of RhB is degraded when just H_2O_2 is used. According to Ouyang et al., the mesoporous CeO_2 has adsorptive capacity for dyes [35]. Therefore, we can conclude that the removal of RhB on the mesoporous 45%Ce—Pr—O solid solution is mainly due to its adsorption. However, RhB was nearly degraded in the presence of H_2O_2 and 45%Ce—Pr—O simultaneously, indicating that the synergistic effect of H_2O_2 and Ce—Pr—O can enhance the efficiency of photocatalysis. The reason may be that H_2O_2 can be easily adsorbed on the surface of Ce—Pr—O because of the oxygen vacancies, inducing the appearance of intermediate products such as O_2^{2-} and/or $Ce(O_2)^+$, which in turn produce active species such as O_2, $O_2^{\bullet-}$, and/or OH to oxidize the target pollutants.

In order to determine the main active species responsible for the photodegradation of RhB, comparison experiments using appropriate reagents as quenchers of possible oxidative intermediate species such as singlet oxygen ($^1O_2$), superoxide ($O_2^{\bullet-}$), hydroperoxy ($HO_2^{\bullet-}$), and/or hydroxyl radical (OH•), were carried out. The quenchers used in the experiments were NaN_3 (a singlet oxygen and/or hydroxyl radical quencher), 1,4-benzoquinone ($C_6H_4O_2$, a quencher of superoxide radical), and KI (a quencher of positive holes, h^+_{VB}, and hydroxyl radical on the catalyst surface), respectively. From the results of comparison experiments, it can be found that NaN_3 and KI did not affect the degradation rate of RhB throughout the experiment (not shown). However, the degradation efficiency of RhB was decreased greatly when $C_6H_4O_2$ was added in the reaction system, as shown in Fig. 13, indicating that the superoxide anion radical is the main oxidative species responsible for the photodegradation of RhB.

According to Koelling et al. [36], the bandgap between the O(2p) valence band (VB) and the Ce(5d) conduction band (CD) is about 6 eV, which make it impossible to transfer the photogenerated electrons from VB to CD. However, the 4f band of CeO_2 plays a vital role for the application of CeO_2 in the photocatalytic reaction due to the Ce(4f), lying within the bandgap, narrow the band, which make the visible light can be absorbed by the ceria easily. Moreover, the oxygen vacancies in the Ce—Pr—O can introduce intermediate energy levels and further decrease the bandgap [37,38], resulting in an efficient visible light absorption. Therefore, under the visible light irradiation, the electrons can be easily excited from VB to Ce(4f) levels and intermediate energy levels resulted from oxygen vacancies. Based on the above analysis, the possible photocatalytic process may be described as follows. RhB adsorbed on the surface of catalyst and irradiated by daylight injects an electron into the Ce(4f) orbital and then this electron is transferred to the oxygen vacancy. On the other hand, electrons are excited from the valence band (VB) to the Ce(4f) orbital and then trapped by the oxygen vacancy to form donors, producing holes in VB. These holes may play a certain role in the recycle of Ce^{3+} and Ce^{4+} due to their strong oxidation. Furthermore, the excited electrons are also directly captured by the intermediate energy levels. As described above, H_2O_2 is mainly adsorbed on the oxygen vacancies of the mesoporous Ce—Pr—O surface and then oxygen (electron acceptor) was accompanied by the recycle of Ce^{3+} and Ce^{4+} in the presence of H_2O_2. The combination of the donor and the acceptor thus produce the active species

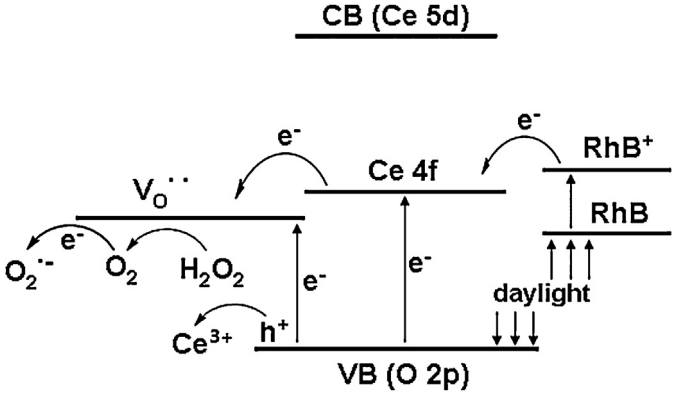

Fig. 14. Proposed photocatalytic mechanism over the mesoporous Ce—Pr—O under the irradiation of daylight ($V_O^{\bullet\bullet}$: oxygen vacancy, h^+: hole, VB: valence band, CB: conduction band).

$\left(O_2^{\bullet-}\right)$ to oxidize the pollutant (RhB) on the surface of mesoporous Ce—Pr—O. Therefore, the possible photocatalytic mechanism of RhB over the mesoporous CeO_2 doped with Pr can be illustrated by the schematic diagram of energy band of CeO_2, as shown in Fig. 14.

4. Conclusions

Mesoporous ceria doped with Pr (Ce—Pr—O) with an ordered 2D hexagonal structure was successfully synthesized in this study. It was found that mesoporous Ce—Pr—O demonstrated a remarkable visible light absorption and numerous oxygen vacancies. Due to the formation of oxygen vacancies, the adsorbed amount of H_2O_2 is greatly increased, which is important to produce active species and then to degrade pollutants. As a photocatalyst, mesoporous Ce—Pr—O exhibited a good performance on the degradation of RhB under weak daylight irradiation, indicating that it has promising practical applications.

Acknowledgment

The financial support by the Natural Science Foundation of Zhejiang Province, China (LY14B070006, Y4110289) is gratefully acknowledged.

References

[1] Y. Jiao, F. Wang, X. Ma, Q. Tang, K. Wang, Y. Guo, L. Yang, Microporous Mesoporous Mater. 176 (2013) 1–7.
[2] R.K. Nagarale, U. Hoss, A. Heller, J. Am. Chem. Soc. 134 (2012) 20783–20787.
[3] B. Yan, W. Zhao, Mater. Sci. Eng., B 110 (2004) 23–26.
[4] X. Feng, D.C. Sayle, Z.L. Wang, M.S. Paras, B. Santora, A.C. Sutorik, T.X.T. Sayle, Y. Yang, Y. Ding, X. Wang, Y.S. Her, Science 312 (2006) 1504–1508.
[5] J.E. Fallah, L. Hilaire, M. Romeo, F.L. Normand, J. Electron Spectrosc. Relat. Phenom. 73 (1995) 89–103.
[6] A.B. Jorge, Y. Sakatani, C. Boissiere, C. Laberty-Roberts, G. Sauthier, J. Fraxedas, C. Sanchez, A. Fuertes, J. Mater. Chem. 22 (2012) 3220–3226.
[7] T. Feng, X. Wang, G. Feng, Mater. Lett. 100 (2013) 36–39.
[8] F. Chen, X. Shen, Y. Wang, J. Zhang, Appl. Catal., B: Environ. 121–122 (2012) 223–229.
[9] Y. Li, Q. Sun, M. Kong, W. Shi, J. Huang, J. Tang, X.C. Zhao, J. Phys. Chem. C 115 (2011) 14050–14057.
[10] T.Y. Ma, Z.Y. Yuan, J.L. Cao, Eur. J. Inorg. Chem. 5 (2010) 716–724.
[11] P. Ji, J. Zhang, F. Chen, M. Anpo, J. Phys. Chem. C 112 (2008) 17809–17813.
[12] Z. Ji, X. Shen, M. Li, H. Zhou, G. Zhu, K. Chen, Nanotechnology 24 (2013) 115603–115611.
[13] S. Hu, F. Zhou, L. Wang, J. Zhang, Catal. Commun. 12 (2011) 794–797.
[14] W. Cai, F. Chen, X. Shen, L. Chen, J. Zhang, Appl. Catal., B: Environ. 101 (2010) 160–168.
[15] D. Channei, B. Inceesungvorn, N. Wetchakun, S. Phanichphant, A. Nakaruk, P. Koshy, C.C. Sorrelld, Ceram. Int. 39 (2013) 3129–3134.
[16] J. Qian, F. Chen, F. Wang, X. Zhao, Z. Chen, Mater. Res. Bull. 47 (2012) 1845–1848.
[17] P. Ji, J. Zhang, F. Chen, M. Anpo, Appl. Catal., B: Environ. 85 (2009) 148–154.
[18] Z. Bian, J. Zhu, S. Wang, Y. Cao, X. Qian, H.S. Li, J. Phys. Chem. C 112 (2008) 6258–6262.
[19] S. Hao, H. Chang, Q. Xiao, Y. Zhong, W. Zhu, J. Phys. Chem. C 115 (2011) 12873–12882.
[20] V.G. Keramidas, W.B. White, J. Chem. Phys. 59 (1973) 1561–1562.
[21] M.F. Luo, Z.L. Yan, L.Y. Jin, J. Mol. Catal., A: Chem. 260 (2006) 157–162.
[22] H.Z. Bao, X. Chen, J. Fang, Z.Q. Jiang, Catal. Lett. 125 (2008) 160–167.
[23] S. Lutkehoff', M. Neumann, Phys. Rev. B: Condens. Matter 52 (1995) 13808–13811.
[24] J.C. Yu, X.C. Wang, X.Z. Fu, Chem. Mater. 16 (2004) 1523–1530.
[25] G. Li, D. Zhang, J.C. Yu, Chem. Mater. 20 (2008) 3983–3992.
[26] J.W. Tang, Z.G. Zou, J.H. Ye, Chem. Mater. 16 (2004) 1644–1649.
[27] J.C. Yu, G.S. Li, X.C. Wang, X.L. Hu, C.W. Leung, Z.D. Zhang, Chem. Commun. (2006) 2717–2719.
[28] F.H. Scholes, A.E. Hughes, S.G. Hardin, P. Lynch, P.R. Miller, Chem. Mater. 19 (2007) 2321–2328.
[29] F.H. Scholes, C. Soste, A.E. Hughes, S.G. Hardin, P.R. Curtis, Appl. Surf. Sci. 253 (2006) 1770–1780.
[30] K. Dimos, P. Stathi, M.A. Karakassides, Y. Deligiannakis, Microporous Mesoporous Mater. 126 (2009) 65–71.
[31] S. Hao, Y. Zhong, P. Francesco, W. Zhu, Chem. Eng. J. 189–190 (2012) 160–167.
[32] Q. Wang, C. Chen, D. Zhao, W. Ma, J. Zhao, Langmuir 24 (2008) 7338–7345.
[33] S. Jum, G.K. Hyun, S.H. Lee, J. Phys. Chem. Solids 73 (2012) 1372–1377.
[34] Y. Hu, X. Gao, L. Yu, Y. Wang, J. Ning, S. Xu, X.W. Lou, Angew. Chem. Int. Ed. 52 (2013) 5636–5639.
[35] X. Ouyang, W. Li, S. Xie, T. Zhai, M. Yu, J. Gan, X. Lu, New J. Chem. 37 (2013) 585–588.
[36] D.D. Koelling, A.M. Boring, J.H. Wood, Solid State Commun. 47 (1983) 227–232.
[37] Y.S. Chaudhary, S. Panigrahi, S. Nayak, B. Satpati, S. Bhattacharjee, N. Kulkarnic, J. Mater. Chem. 20 (2010) 2381–2385.
[38] J. Dong, J. Han, Y. Liu, A. Nakajima, S. Matsushita, S. Wei, W. Gao, ACS Appl. Mater. Interfaces 6 (2014) 1385–1388.